Article

Structure

Structural Basis for Glycerol Efflux and Selectivity of Human Aquaporin 7

Graphical Abstract

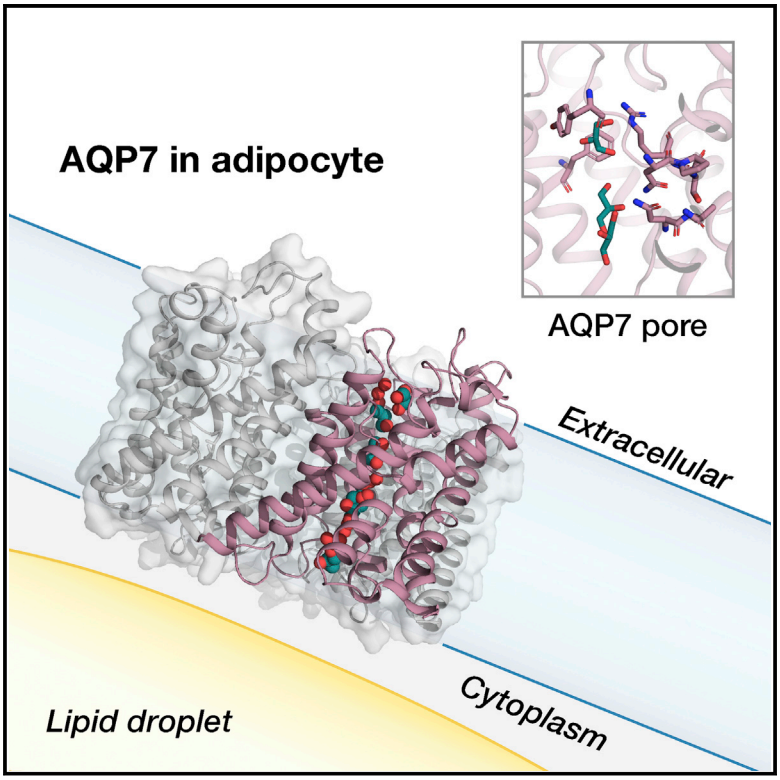

Highlights

- X-ray structure of human AQP7 at 1.9 Å resolution
- Glycerol hinders high water flux through AQP7
- Rotation of glycerols in the pore suggest a novel conducting mechanism

Authors

Sofia W. de Maré,
Raminta Venskutonytė,
Sandra Eltschkner, Bert L. de Groot,
Karin Lindkvist-Petersson

Correspondence

karin.lindkvist@med.lu.se

In Brief

AQP7 is an important glycerol channel in human adipocytes, and its dysfunction is linked to metabolic disorders. The high-resolution X-ray structures of AQP7 unravels the molecular details of how glycerol travels through the channel and provide a structural basis for development of small-molecule drugs for targeting AQP7.

de Maré et al., 2020, Structure *28*, 215–222
February 4, 2020
https://doi.org/10.1016/j.str.2019.11.011

CellPress

Structure
Article

Structural Basis for Glycerol Efflux and Selectivity of Human Aquaporin 7

Sofia W. de Maré,[1] Raminta Venskutonytė,[1] Sandra Eltschkner,[1] Bert L. de Groot,[2] and Karin Lindkvist-Petersson[1,3,*]
[1]Experimental Medical Science, Medical Structural Biology, BMC C13, Lund University, SE-221 84 Lund, Sweden
[2]Department of Theoretical and Computational Biophysics, Max Planck Institute for Biophysical Chemistry, Göttingen, Germany
[3]Lead Contact
*Correspondence: karin.lindkvist@med.lu.se
https://doi.org/10.1016/j.str.2019.11.011

SUMMARY

The aquaglyceroporin 7 (AQP7) facilitates permeation of glycerol through cell membranes and is crucial for lipid metabolism in humans. Glycerol efflux in human adipocytes is controlled by translocation of AQP7 to the plasma membrane upon hormone stimulation. Here we present two X-ray structures of human AQP7 at 1.9 and 2.2 Å resolution. The structures combined with molecular dynamics simulations suggest that AQP7 is a channel selective for glycerol and that glycerol may hamper water permeation through the channel. Moreover, the high resolution of the structures facilitated a detailed analysis of the orientation of glycerol in the pore, disclosing unusual positions of the hydroxyl groups. The data suggest that glycerol is conducted by a partly rotating movement through the channel. These observations provide a framework for understanding the basis of glycerol efflux and selectivity in aquaglyceroporins and pave the way for future design of AQP7 inhibitors.

INTRODUCTION

Adipose tissue plays a key role in storage and mobilization of energy in the body, and adipocytes store energy as triacylglycerides (TAGs) in a single large lipid droplet (Hansen et al., 2017). During states of increased energy demands, such as fasting and exercise, adipocyte lipolysis is increased causing release of glycerol and free fatty acids. The aquaglyceroporin AQP7 is highly expressed in adipocytes and facilitates efflux of glycerol by passive diffusion (Maeda et al., 2004). The diameter of human adipocytes can vary between 70 and 120 μm, depending on whether the individual is lean or obese. Therefore, a major component of metabolic flexibility is the ability of the adipocyte to adjust its volume depending on fluctuations in the amount of stored lipids (Le Lay et al., 2015). Because of this property of adipocytes, AQP7 deficiency has been linked to TAG accumulation in adipose tissue leading to adipocyte hypertrophy, confirming the importance of AQP7 for human lipid metabolism (Hara-Chikuma et al., 2005).

The human genome encodes four aquaglyceroporins AQP3, AQP7, AQP9, and AQP10, all belonging to the family of aquaporins. Whether all four are expressed in human adipocytes has been debated (Miranda et al., 2010; Rodriguez et al., 2011). At the mRNA level, AQP7 is significantly higher expressed in subcutaneous adipose tissue compared with AQP10 (Laforenza et al., 2013). However, a recent structural and functional study of AQP10 suggests that AQP10 facilitates the transport of glycerol in a pH-dependent manner in adipocytes (Gotfryd et al., 2018). In contrast, AQP7 has been shown to have the same glycerol activity at both high and low pH (pH 6–8) (Katano et al., 2014b; Palmgren et al., 2017) and to regulate glycerol efflux in adipocytes by a hormonally controlled trafficking mechanism, i.e., shuttling between the lipid droplet and the plasma membrane (Rodriguez et al., 2011). Explicitly, AQP7 binds to Perilipin 1 (PLIN1) under lipogenic conditions, which is a protein decorating the lipid droplet in adipocytes (Hansen et al., 2016; Londos et al., 1999). The binding is significantly reduced when AQP7 is phosphorylated by protein kinase A (PKA), suggesting that AQP7 is held by PLIN1 at the lipid droplet under lipogenic conditions, while at lipolytic conditions when PKA is activated, AQP7 becomes phosphorylated and translocate to the plasma membrane for glycerol efflux (Hansen et al., 2016; Iena and Lebeck, 2018).

The role of AQP7 as a glycerol efflux channel is well described in the literature; however, it is still debated whether it also facilitates the transport of water at similar rates as the orthodox aquaporins (strict water channels) (Kondo et al., 2002; Palmgren et al., 2017). Thus, to clarify the functional mechanism of human AQP7, we determined two X-ray structures of AQP7 at 1.9 and 2.2 Å resolution and performed molecular dynamics (MD) simulations of the glycerol passage through the pore of AQP7. The combined results provide a structural framework that contributes to the understanding of glycerol selectivity of AQP7. The structure shows an open channel with well-ordered glycerol and water molecules lining the pore. Interestingly, close to the two structural hallmarks of aquaporins, the aromatic/arginine selectivity filter and the NPA signature motifs, the glycerol molecules form a hydrogen bond network characterized by partly turning the hydroxyl groups toward the more hydrophobic side of the pore. This suggests a conducting mechanism for glycerol based on the rotation of the molecule. Moreover, MD simulations show a significantly reduced osmotic permeability coefficient for water in the presence of glycerol, suggesting that glycerol prevents an unrestricted flux of water through human AQP7.

RESULTS

X-ray Structure of Human AQP7 at 1.9 Å Resolution

Two complete datasets were collected from two single crystals and the three-dimensional structures of human AQP7 were

Table 1. Crystallographic Data and Refinement Statistics

	Crystal 1–1.9 Å	Crystal 2–2.2 Å
Data Collection		
Wavelength	0.976	0.976
Space group	I4	I4
Unit cell dimensions		
a, b, c (Å)	85.83, 85.83, 83.05	86.76, 86.76, 83.53
Resolution (Å)	60.69–1.90 (1.94–1.90)	61.35–2.20 (2.27–2.20)
R_{merge}	0.037 (1.57)	0.025 (0.517)
I/σI	20.4 (1.1)	17.2 (1.5)
CC1/2[a]	0.402	0.788
Completeness (%)	100 (99.5)	98.8 (99.6)
Redundancy	6.7 (5.4)	3.3 (3.4)
Refinement		
Resolution (Å)	41.53–1.90	41.77–2.20
No. of reflections	23,744	15,532
R_{work}/R_{free}	0.172/0.195	0.209/0.243
No. of atoms		
Protein	1,908	1,868
Glycerol	84	66
Water	39	12
B factors (Å^2)		
Protein	58.49	85.90
Glycerol	76.88	89.80
Water	58.52	75.12
Root-mean-square deviation		
Bond lengths (Å)	0.003	0.004
Bond angles (°)	0.574	0.600
Ramachandran plot (%)		
Favored	96	96
Outliers	0.82	0.82

Data for outer resolution shell in parentheses.
[a]Outer shell only.

determined at 1.9 Å (crystal 1) and 2.2 Å (crystal 2), where crystal 1 had been exposed to gradient increase of glycerol up to 20% and crystal 2 to 5% glycerol, before freezing (Table 1). Wild-type AQP7 did not yield well-diffracting crystals; however, the truncated version (amino acids 33–279) crystallized in space group I4 with one monomer in the asymmetric unit and the crystallographic axis coinciding with the physiological 4-fold axis of the aquaporin tetramer. All residues could be modeled in the high-resolution structure (1.9 Å), and residues 34–278 could be modeled in the lower-resolution structure (2.2 Å).

Overall, the differences between the two structures are minimal, with a root-mean-square deviation of 0.83 Å. The AQP7 monomer follows the canonical aquaporin fold of a right-handed bundle consisting of six transmembrane helices and two half-membrane spanning helices (M1-M8) (Figures 1A and 1B). In addition, there are five loops connecting the helices, loop A, C, E on the extracellular side, and loop B and D on the intracellular side. There are two particularly conserved regions within the aquaporin family, the aromatic/arginine (ar/R) selectivity filter and the two NPA motifs (Asn-Pro-Ala), the signature motifs of aquaporins (Figures 1C and 1D). Interestingly, the human AQP7 has unusual NPA motifs, where both the asparagines are conserved but rare substitutions create NAA (Asn94, Ala95, and Ala96) and NPS (Asn226, Pro227, and Ser228) motifs. The selectivity filter, situated in the extracellular vestibule of the aquaporin, is known to be wider in the aquaglyceroporins compared with the orthodox aquaporins, to facilitate the transport of the larger glycerol molecule. This is also seen in AQP7 in which the selectivity filter has a diameter of 3.3 Å according to the HOLE analysis (Figure 1A). The selectivity filter is amphipathic and the hydrophobic corner previously described in the structures of aquaglyceroporins from *Escherichia coli* (GlpF) and *Plasmodium falciparum* (PfAQP) is structurally conserved in AQP7 (Figure S1A) (Fu et al., 2000; Newby et al., 2008). In both GlpF and PfAQP, the hydrophobic corners are created by a tryptophan and a phenylalanine, while in AQP7 the tryptophan is replaced by a phenylalanine (Phe74), and the phenylalanine is replaced by a tyrosine (Tyr223), whereas the arginines in the ar/R are completely overlapping in all three structures (Figure S1A). Another feature of aquaporins is the pseudo-helix that is created by two half-membrane helices M3 and M7 (Figure 1A) connected by the NPA motifs (Figure 1D). Superimposing the structure of AQP7 with GlpF reveals that the conserved asparagine side chains are structurally overlapping, although the stacking between the two prolines is absent (because one proline is absent in AQP7) (Figure S1B). Instead, a hydrogen bond is formed between the serine (Ser228) in NPS and the backbone nitrogen of the alanine (Ala95) in NAA to stabilize the asparagines in optimal positions for glycerol efflux and maintenance of the structural organization of the seventh pseudo-helix (Figure 1).

Glycerol Is Conducted by a Partly Rotating Movement through the Channel

Five glycerol molecules (G1-G5) were modeled in the extracellular and intracellular vestibules of the conducting pore of the AQP7 structure exposed to 20% glycerol (1.9 Å), and four (G2-G5) were modeled in the structure that was exposed to 5% glycerol (2.2 Å), in positions where the electron density could not account for water molecules only (Figures S2 and S5). The G2-G5 glycerol molecules were placed in similar positions for both structures (Figure S2). Just above the selectivity filter, in the extracellular vestibule, one glycerol molecule (G2) was fitted in both structures with potential hydrogen bonds to the NH2 of Arg229 and to the carbonyl oxygen of Gly222. In addition, another glycerol molecule G1 was fitted above G2 in the high-resolution structure (Figure S2A).

In the selectivity filter, clear electron density could be accounted for by one glycerol molecule (G3) in both structures (Figures 2A and 2B), which is bound through an extended network of hydrogen bonds. In the high-resolution structure, G3 can interact with the backbone oxygen of Tyr223 via O1 and serves as a hydrogen bond acceptor for the guanidino group of Arg229. In the lower-resolution structure, O1 makes the same contacts to Tyr223 and can also hydrogen bond to N_ϵ of Arg229 (Figures 2A, 2B, and S3). The O3 establishes hydrogen bonds to the backbone of Ala224 in both structures as well as to the neighboring water or glycerol molecule closer to the NPA region of the pore (Figures 2 and S3). The O2 is less defined and is trapped

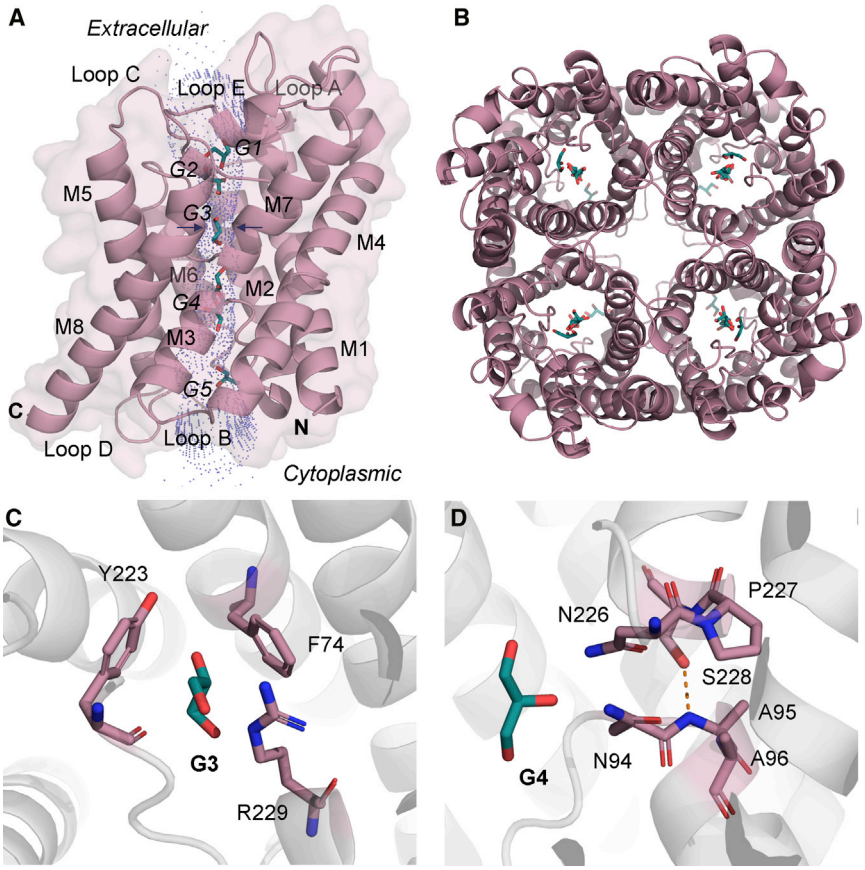

Figure 1. The Overall Structure of Human AQP7

(A) Cartoon representation of a monomer with the six helices and two half-helices (M1-M8), two intracellular loops (loops B and D) and three extracellular loops (loops A, C, and E). Five glycerol molecules (G1–G5, teal) shown as sticks are present in the conducting pore, diameter calculated by the HOLE program, and represented by blue dots. Arrows indicate the selectivity filter with a diameter of 3.3 Å.

(B) Top view of the AQP7 tetramer seen from the extracellular side.

(C) Residues (pink) and glycerol (teal) in the ar/R selectivity filter shown as sticks.

(D) The NPA motifs in AQP7 shown as sticks (pink) and glycerol in teal, hydrogen bond indicated by orange dashed line.

between the two aromatic side chains of Phe74 and Tyr223 in the selectivity filter. Interestingly, the O2 forms a hydrogen bond to the OH group of Tyr223, which in GlpF and PfAQP is replaced by a phenylalanine which does not provide the possibility of hydrogen bond formation. Hence, the orientation of O2 of G3 is a unique feature of the AQP7 selectivity filter (Figures 2 and S3). In both structures, O1 is within hydrogen bond distance to the backbone carbonyl oxygens of both Gly222 and Tyr223. However, the distance toward the backbone oxygen of Tyr223 is slightly favored in both structures, although the possibility of equilibrium between the interactions of O1 with either Gly222 or Tyr223 cannot be ruled out.

In the NAA/NPS region of AQP7, an extended electron density is observed in the structures (Figures 2C, 2D, and S3). The crystallization condition contained PEG 200. To distinguish whether glycerol or PEG 200 is the better model for the extended density the unbiased electron densities after initial refinement cycles were also evaluated (Figures S4A–S4D). As seen in Figure S4, the shape of the densities suggests the presence of two molecules, not one long extended molecule (Figures S4E and S4F). The hydrogen bond network to the surrounding residues is less favorable for PEG 200 compared with the glycerol molecules (Figures S4G–S4J; Table S1). In particular, PEG 200 modeled in the structure exposed to low glycerol concentrations (and potentially more likely to have PEG 200 in the pore), cannot participate in any hydrogen bonding to the residues (Figure S4I). In addition, PEG 200 clashes with Asn94 in the high-resolution structure (Figure S4G) and $F_o - F_c$ omit maps for both structures do not support the presence of an entire PEG 200 molecule (Figures S4C and S4D). The R-factors for the structures refined with glycerol or PEG 200 were 0.172/0.195 or 0.164/0.200 for the high-resolution structure, and 0.209/0.243 or 0.217/0.245 for the lower-resolution structure. Based on these observations, we cannot exclude the possibility of PEG 200 in the pore, but we believe that glycerol is a more descriptive model of the density. Hence, two alternative positions of the glycerol molecule G4 were modeled into this density, together with one or two water molecules in the lower- and high-resolution structures, respectively (Figures 2C, 2D, and S3). One G4 alternative (G4a) could be well accommodated in the density within hydrogen bond distance to either of the asparagine side chains in the NPA motifs in the high-resolution structure (Figure 2C), or to the side chain of Asn226 only and the backbone carbonyl oxygen of Met93 in the lower-resolution structure (Figure S3A). The G4a in the high-resolution structure displays an additional water-bridged hydrogen bond to the carbonyl oxygen of His92 (Figure 2C). In contrast, G4a in the lower-resolution structure is slightly rotated thereby losing the potential interaction with Asn94. Because of the slight downward movement of G4a in the lower-resolution structure, compared with the high-resolution structure, G4a can directly interact with the backbone of His92 and form a potential water-bridged hydrogen bond to the backbone carbonyl of Ala91 (Figure S3A).

The other alternative position of the glycerol at the NPA motifs (G4b) was modeled closer to the intracellular vestibule in the extended density (Figures 2D, S3B, and S5). This alternative position of glycerol depicts a more loosely bound state of a glycerol molecule entering from the intracellular vestibule. In the high-resolution structure, O1 of G4b is still within hydrogen bond distance to the side chain of Asn94, and the site for G4a would in this case be occupied by one of the water molecules to bridge the gap between two subsequently traversing glycerol molecules (G3 and G4b). Moreover, G4b in the lower-resolution structure is not hydrogen bonding to the asparagines but instead to

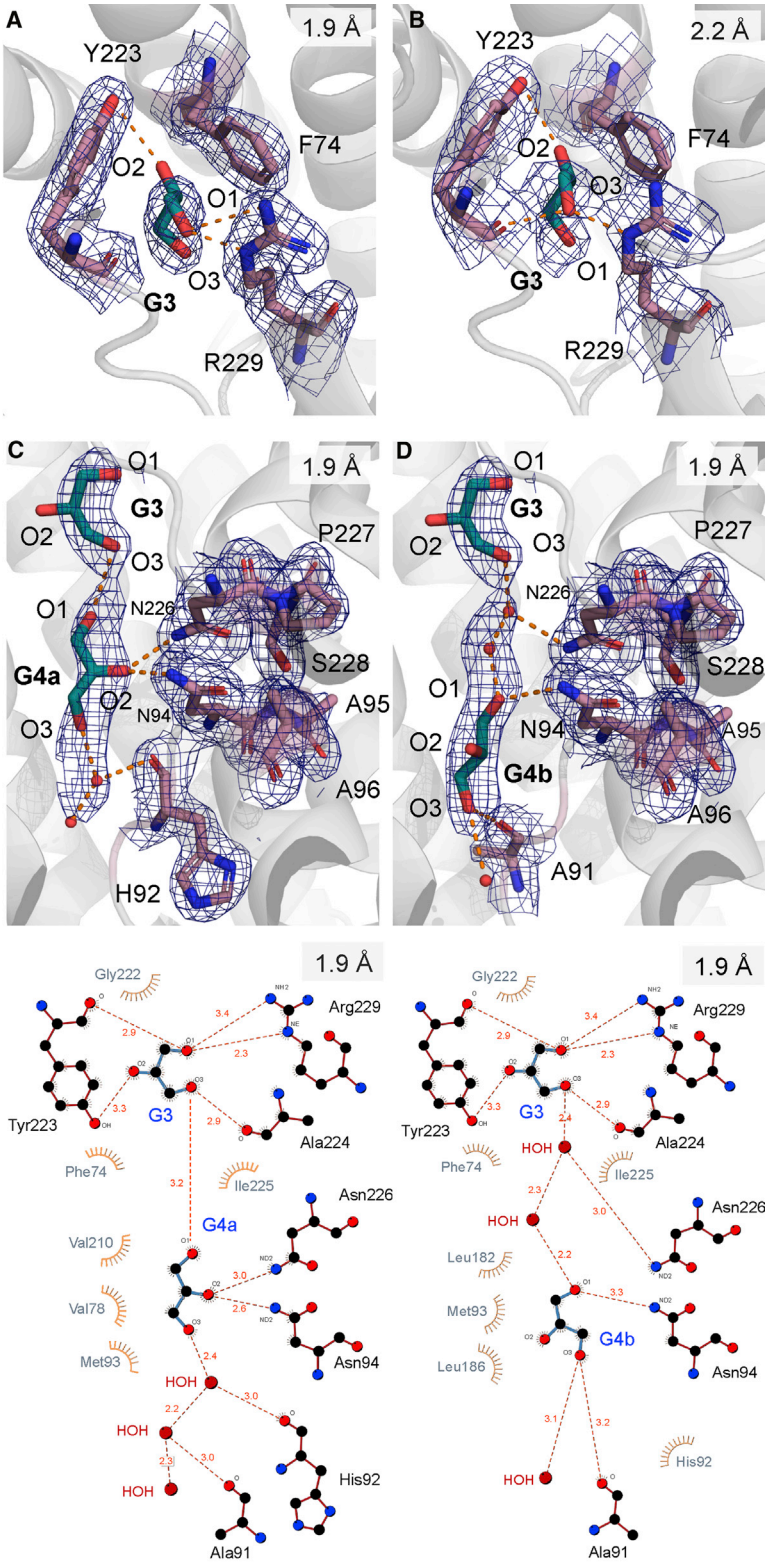

Figure 2. The Hydrogen Bond Network of Glycerol and Water Molecules in the Conducting Pore of AQP7

(A and B) Glycerol G3 in the selectivity filter of the high-resolution (A) and lower-resolution (B) structures.

(C and D) Glycerol G4 in two alternative positions in the NPA region of the high-resolution structure. Stick representation of the residues (pink) and glycerol (teal) with the backbone represented by cartoon drawing (gray). Dashed lines indicate hydrogen bonds within 3.4 Å. Lower panels show the hydrogen bond network of water and glycerol in 2D representation. $2F_o - F_c$ electron density maps contoured at 1σ.

the backbone oxygen of His92, which is part of the exposed carbonyl groups of Gly90 and His92 that flank the pore (Figure S3B). The switch between the two positions at the NPA region is either accompanied or induced by a rotation of the molecule, which can be observed in both structures. Interestingly, the two alternative glycerol molecules G4a and the G4b each refine to occupancies of close to 50% (45% for G4a and 55% for G4b), suggesting the NPA area to be a "transition point" for glycerol through the pore.

Glycerol Hinders Rapid Water Permeation

To address the question of water and glycerol permeation, atomistic MD simulations were carried out for the AQP7 tetramer embedded in a POPC bilayer membrane. Three different scenarios were considered: a water-only and glycerol-free environment, a setup with 16 glycerol molecules starting in the bulk phase, and a setup with 16 glycerol molecules (4 per monomer) initially bound to their crystallographic positions. The crystallographic conformation was found to be highly permeable to water, with a computed osmotic permeability coefficient (pf) = $4.8 \pm 0.2 \times 10^{-14}$ cm^3/s, as can be seen in Figure 3A; whereas in the presence of glycerol, the water permeability is significantly reduced by a factor of 2–4. The water permeability in the presence of glycerol can only be approximately determined from MD simulations at the μs timescale because of the slow exchange of glycerol positions, and the according dependence of the initial placement of the glycerol molecules. We expect it to be in the range between 1.3 and 2.4 × 10^{-14} cm^3/s, the values obtained with all glycerol molecules initially bound in their crystallographic positions, and with all glycerol molecules initially in bulk, respectively. Both the lack of complete unbinding as well as spontaneous binding on the microsecond timescale indicate a high glycerol affinity, responsible for a hindered water permeation in the presence of glycerol. In total, 14 glycerol association and 66 dissociation events were recorded. This indicates a rapid exchange of glycerol molecules allowing efficient permeation. The potential of mean force (PMF) for glycerol in the channel provides further insight into the determinants of glycerol permeation (Figure 3B). Overall, the maximum barrier of about 8 kJ/mol is lower than that observed for GlpF (Hub and de Groot, 2008) and consistent with efficient permeation. In addition, the positions

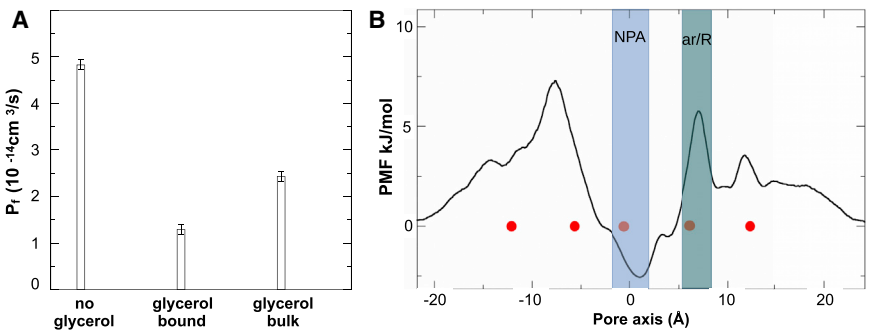

Figure 3. Osmotic Water Permeability and Glycerol Potential of Mean Force of AQP7 from MD Simulations

(A) Osmotic water permeability coefficients (Pf) from MD simulation in the absence of glycerol (left), with 16 glycerol molecules initially bound to their crystallographic positions (center) and with 16 glycerol molecules initially positioned in bulk solution (right). Error bars represent ± SEM.

(B) Glycerol potential of mean force from MD simulation as obtained from the glycerol central carbon atom number density and the Boltzmann relation. The red dots mark the crystallographically determined glycerol positions.

of crystallographically determined glycerol positions (red dots) agree favorably with the PMF in the sense that the crystallographic positions correspond to low and bulk-like free energy regions, leaving high free energy (barrier) regions unsampled, consistent with the high glycerol concentration crystallographic conditions. It is interesting to note that, although the ar/R selectivity filter is the narrowest part of the channel, the major barrier is found on the intracellular side of the NPA region characterized by the hydrophobic residues Val82, Met93, and Leu186.

DISCUSSION

Aquaporin 7 is known to play a central role for human energy metabolism and is abundantly expressed in human adipocytes, where it controls glycerol efflux (Iena and Lebeck, 2018). AQP10 has also been suggested to be important for regulation of glycerol efflux in human adipocytes (Gotfryd et al., 2018). Analysis of the channels by the HOLE program shows that AQP7 has a diameter of around 3 Å at the selectivity filter, while AQP10 is much wider, around 5 Å, due to the lack of the bulky amino acids of the hydrophobic corner, suggesting that AQP10 could potentially accommodate an even wider range of molecules larger than glycerol (Figure 4).

Moreover, in contrast to AQP7, in which the narrowest part of the pore coincides with the selectivity filter, the AQP10 has a narrowing on the intracellular side of the pore that permits water flux but does not allow the passage of glycerol (Gotfryd et al., 2018) (Figure 4). These significant differences between the two human aquaglyceroporins imply a different mechanism of glycerol regulation as well as different physiological activity. Indeed, it has been suggested that AQP10 is regulated in a pH-dependent manner, with His80 in AQP10 being a key residue acting as a gate (Gotfryd et al., 2018). This histidine (His92 in AQP7) is sequentially conserved among the human aquaporins, and AQP10 is the only one with increased activity upon pH reduction (Gotfryd et al., 2018), indicating that the presence of a histidine in this position cannot solely explain the gating mechanism of AQP10. Gotfryd and co-workers suggest that His80 in AQP10 is a pH sensor and undergoes structural rearrangements due to its double protonation at low pH (pH 5) leading to the opening of the channel (Gotfryd et al., 2018). Interestingly, a phenylalanine residue in AQP10 (Phe85) is part of the narrowing of the channel and is not conserved in AQP7, where a valine (Val97) is present at this position instead, which results in a wider diameter of the pore in this part of the channel. Thus, although crucial residues in the pore area are conserved within the aquaporin family, it is clear from the available structures that minor differences result in significant different structural and functional outcome.

In the other previously structurally determined aquaglyceroporins (GlpF, PfAQP, and AqpM) (Fu et al., 2002; Lee et al., 2005; Newby et al., 2008), the typical hydrophobic corner as well as an open conformation toward the intracellular side is observed, as in AQP7. All structures show a pattern of alternating glycerol-water molecules in the pore, although in varying order and numbers (Figure S2). However, AqpM and AQP10 may have different conducting mechanisms or different substrate specificities as they both have only a single glycerol molecule in the pore situated in the NPA region and no glycerol present in the selectivity filter. In addition, they display high water permeability, in comparable rates with orthodox aquaporins (Gotfryd et al., 2018; Lee et al., 2005). AQP7, on the other hand, has glycerol bound in both the ar/R selectivity filter and at the NPA motifs, where, in the latter, glycerol is present in two alternative positions, indicating the flexibility of the interactions with the residues in the NPA region. In addition, besides glycerol molecules observed at the NPA motif and in the selectivity filter, another glycerol molecule, G5, was observed in the vestibule on the cytoplasmic side. Glycerol molecules in similar positions are also observed in the structures of PfAQP and AqpM. Interestingly, in both these structures an increase in local glycerol concentration in the extracellular vestibule is described as possibly important for glycerol conductance (Lee et al., 2005; Newby et al., 2008), and the presence of glycerol in the intracellular vestibules could potentially have the same function for AQP7, as AQP7 mainly functions as an efflux channel. G5 is in contact with the glycerol at the NPA motifs via water-bridged hydrogen bonding. Following the pathway of glycerol from the intracellular to the extracellular spaces, the position of G4b in the lower-resolution structure displays an initial state of a glycerol molecule entering the pore. G4b forms a hydrogen bond to the backbone oxygen of His92, which is part of the exposed carbonyl groups that flank the pore. Here, the glycerol molecule is not yet within hydrogen-bonding distance to the asparagine side chains of the NPA motifs. In contrast, in the high-resolution structure, G4b is positioned closer to the NPA region and is within hydrogen-bonding distance to Asn94. Further along the pore, in the alternative position G4a, the glycerol is located closer to the NPA motifs. In the lower-resolution structure it establishes hydrogen bonds with Met93 and Asn226, before engaging into a tightly coordinated state bound to both asparagines of the NPA motifs, observed in the

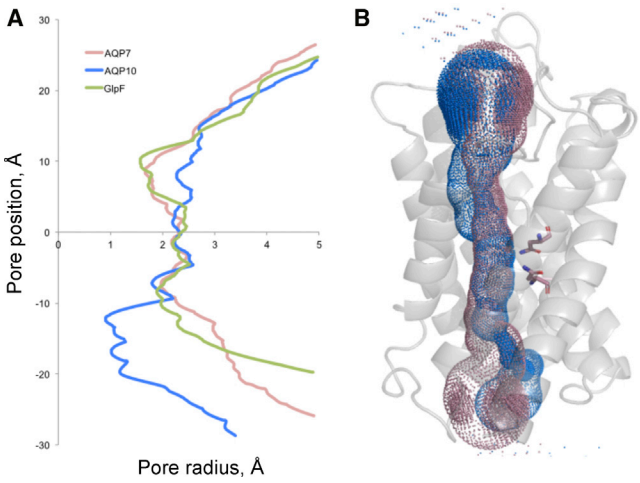

Figure 4. HOLE Analysis of AQP7, GlpF, and AQP10

(A). Radii along the pore for AQP7 (pink), GlpF (green), and AQP10 (blue), from extracellular to intracellular side, top to bottom. Pore position 0 set to the center of the NPA region.

(B) Dot representation of the HOLE analysis AQP7 (pink) and AQP10 (blue) placed in cartoon representation of AQP7 (gray). Residues of AQP7 represented by sticks (pink).

high-resolution structure. The reorientation of O2 from the apolar side of the pore in G4b, to the polar side of the pore in G4a, could indicate a potential guiding mechanism for incoming glycerol molecules moving toward the NPA motifs. The rotation of the glycerol molecule might facilitate its transition from one position to the other, as well as the associated alteration of the hydrogen bond network. Steered MD simulations of glycerol in GlpF have shown that stereoselectivity for glycerol resulted in different amounts of force required to pull glycerol through the channel (Jensen et al., 2002). This supports an efflux mechanism of glycerol in which rotation of glycerol serves to break hydrogen bonds and to thus release the glycerol from more tightly bound positions and allowing it to move along the pore. In addition, the co-transport of water molecules is strictly required for glycerol conduction, since water and glycerol compete for hydrogen-bonding sites in the channel interior (Jensen et al., 2001, 2002). Together with the rotation of glycerol, this might be crucial to facilitate glycerol release from aquaglyceroporins with highly specific binding positions for glycerol combined with high affinity for glycerol, as in the case of AQP7 and GlpF. When the glycerol has passed through the NPA region and the selectivity filter, it is released into the extracellular space. The previously described position of G2 represents an almost complete detachment of glycerol from the selectivity filter. The mainly hydrophobic environment of the extracellular vestibule accompanied by a lack of hydrogen-bonding partners for the hydroxyl groups of glycerol may facilitate glycerol release from the pore.

Compared with the orthodox aquaporins, AQP7 has been shown to have significantly lower water permeability in cell-based assays (Katano et al., 2014b; Palmgren et al., 2017). However, the water permeability of human AQP7 was recently measured in a proteopolymerosome assay in which AQP7 was shown to have similar water permeability as the orthodox aquaporins (Gotfryd et al., 2018). In a cellular environment glycerol is likely to be present, as opposed to the glycerol-free proteopolymerosome setup (Palmgren et al., 2017). Hence, these experimental results support the MD simulations presented here, showing reduced water permeability of AQP7 in the presence of glycerol.

Finally, there is growing evidence of adipocytes being active players in the tumor microenvironment, and it has been shown that tumors induce lipolysis in adipocytes, resulting in release of glycerol that can be used to fuel tumor growth (Nieman et al., 2011). Hence, AQP7 has become a relevant therapeutic target for tumor therapy. Interestingly, in the X-ray structure of AQP7 a glycerol molecule in the NPA region could be accommodated in two alternative positions, with many possible interactions with the surrounding residues (Figures 2C and 2D). Katano and co-workers have described inhibition of glycerol permeation in human AQP7 by the acyl glycerol derivatives monoacetin, monobutyrin, and diacetin, and the glycerol derivative diglycerol, but not triacetin, which is branched and lacks hydroxyl groups (Katano et al., 2014a). The structures presented here suggest that AQP7 could potentially accommodate prolonged glycerol derivatives, which can be used for inhibitor design to outcompete glycerol.

STAR★METHODS

Detailed methods are provided in the online version of this paper and include the following:

- KEY RESOURCES TABLE
- LEAD CONTACT AND MATERIALS AVAILABILITY
- EXPERIMENTAL MODEL AND SUBJECT DETAILS
  - Heterologous Protein Expression
- METHOD DETAILS
  - Protein Purification
  - Crystallization and Structure Determination
  - HOLE Analysis of the Pore
  - Molecular Dynamics Simulations
- QUANTIFICATION AND STATISTICAL ANALYSIS
  - Software
  - Diffraction Data Collection and Final Refinement
  - Statistical Analysis Molecular Dynamics Simulations
- DATA AND CODE AVAILABILITY
- ADDITIONAL RESOURCES

SUPPLEMENTAL INFORMATION

Supplemental Information can be found online at https://doi.org/10.1016/j.str.2019.11.011.

ACKNOWLEDGMENTS

This work was supported by NordForsk (82000-2), the Swedish Research Council (2016-01319), the Swedish Cancer Foundation (2017/307), and Diabetesfonden (DIA2017-251). We thank PETRA III, MAXIV, ESRF, and SLS for providing beamtime for screening, and data collection at the P13 beamline at PETRA III.

AUTHOR CONTRIBUTIONS

S.W.d.M., K.L.-P., and B.L.d.G. designed the experiments. S.W.d.M. and B.L.d.G. conducted the experiments. S.W.d.M., R.V., S.E., B.L.d.G., and K.L.-P. analyzed the data. S.W.d.M., R.V., S.E., B.L.d.G., and K.L.-P. wrote the manuscript.

DECLARATION OF INTERESTS

The authors declare no competing interests.

Received: May 8, 2019
Revised: October 7, 2019
Accepted: November 15, 2019
Published: December 9, 2019

REFERENCES

Abraham, M.J., Murtola, T., Schulz, R., Páll, S., Smith, J.C., Hess, B., and Lindahl, E. (2015). GROMACS: high performance molecular simulations through multi-level parallelism from laptops to supercomputers. SoftwareX *1*, 19–25.

Adams, P.D., Afonine, P.V., Bunkoczi, G., Chen, V.B., Davis, I.W., Echols, N., Headd, J.J., Hung, L.W., Kapral, G.J., Grosse-Kunstleve, R.W., et al. (2010). PHENIX: a comprehensive Python-based system for macromolecular structure solution. Acta Crystallogr. D Biol. Crystallogr. *66*, 213–221.

Afonine, P.V., Grosse-Kunstleve, R.W., Echols, N., Headd, J.J., Moriarty, N.W., Mustyakimov, M., Terwilliger, T.C., Urzhumtsev, A., Zwart, P.H., and Adams, P.D. (2012). Towards automated crystallographic structure refinement with phenix.refine. Acta Crystallogr. D Biol. Crystallogr. *68*, 352–367.

Bussi, G., Donadio, D., and Parrinello, M. (2007). Canonical sampling through velocity rescaling. J. Chem. Phys. *126*, 014101.

Chen, V.B., Arendall, W.B., 3rd, Headd, J.J., Keedy, D.A., Immormino, R.M., Kapral, G.J., Murray, L.W., Richardson, J.S., and Richardson, D.C. (2010). MolProbity: all-atom structure validation for macromolecular crystallography. Acta Crystallogr. D Biol. Crystallogr. *66*, 12–21.

Cianci, M., Bourenkov, G., Pompidor, G., Karpics, I., Kallio, J., Bento, I., Roessle, M., Cipriani, F., Fiedler, S., and Schneider, T.R. (2017). P13, the EMBL macromolecular crystallography beamline at the low-emittance PETRA III ring for high- and low-energy phasing with variable beam focusing. J. Synchrotron Radiat. *24*, 323–332.

Darden, T., York, D., and Pedersen, L. (1993). Particle mesh Ewald: an N·log (N) method for Ewald sums in large systems. J. Chem. Phys. *98*, 10089–10092.

Emsley, P., Lohkamp, B., Scott, W.G., and Cowtan, K. (2010). Features and development of Coot. Acta Crystallogr. D Biol. Crystallogr. *66*, 486–501.

Evans, P. (2006). Scaling and assessment of data quality. Acta Crystallogr. D Biol. Crystallogr. *62*, 72–82.

Evans, P.R. (2011). An introduction to data reduction: space-group determination, scaling and intensity statistics. Acta Crystallogr. D Biol. Crystallogr. *67*, 282–292.

Fu, D., Libson, A., Miercke, L.J., Weitzman, C., Nollert, P., Krucinski, J., and Stroud, R.M. (2000). Structure of a glycerol-conducting channel and the basis for its selectivity. Science *290*, 481–486.

Fu, D., Libson, A., and Stroud, R. (2002). The structure of GlpF, a glycerol conducting channel. Novartis Found. Symp. *245*, 51–61, discussion 61-5, 165-8.

Gotfryd, K., Mosca, A.F., Missel, J.W., Truelsen, S.F., Wang, K., Spulber, M., Krabbe, S., Helix-Nielsen, C., Laforenza, U., Soveral, G., et al. (2018). Human adipose glycerol flux is regulated by a pH gate in AQP10. Nat. Commun. *9*, 4749.

Hansen, J.S., De Mare, S., Jones, H.A., Goransson, O., and Lindkvist-Petersson, K. (2017). Visualization of lipid directed dynamics of perilipin 1 in human primary adipocytes. Sci. Rep. *7*, 15011.

Hansen, J.S., Krintel, C., Hernebring, M., Haataja, T.J., De Mare, S., Wasserstrom, S., Kosinska-Eriksson, U., Palmgren, M., Holm, C., Stenkula, K.G., et al. (2016). Perilipin 1 binds to aquaporin 7 in human adipocytes and controls its mobility via protein kinase A mediated phosphorylation. Metabolism *65*, 1731–1742.

Hara-Chikuma, M., Sohara, E., Rai, T., Ikawa, M., Okabe, M., Sasaki, S., Uchida, S., and Verkman, A.S. (2005). Progressive adipocyte hypertrophy in aquaporin-7-deficient mice: adipocyte glycerol permeability as a novel regulator of fat accumulation. J. Biol. Chem. *280*, 15493–15496.

Hess, B., Bekker, H., Berendsen, H.J., and Fraaije, J.G. (1997). LINCS: a linear constraint solver for molecular simulations. J. Comput. Chem. *18*, 1463–1472.

Huang, J., Rauscher, S., Nawrocki, G., Ran, T., Feig, M., De Groot, B.L., Grubmüller, H., and Mackerell, A.D., Jr. (2017). CHARMM36m: an improved force field for folded and intrinsically disordered proteins. Nat. Methods *14*, 71.

Hub, J.S., and de Groot, B.L. (2008). Mechanism of selectivity in aquaporins and aquaglyceroporins. Proc. Natl. Acad. Sci. U S A *105*, 1198–1203.

Iena, F.M., and Lebeck, J. (2018). Implications of aquaglyceroporin 7 in energy metabolism. Int. J. Mol. Sci. *19*, https://doi.org/10.3390/ijms19010154.

Jensen, M.O., Park, S., Tajkhorshid, E., and Schulten, K. (2002). Energetics of glycerol conduction through aquaglyceroporin GlpF. Proc. Natl. Acad. Sci. U S A *99*, 6731–6736.

Jensen, M.O., Tajkhorshid, E., and Schulten, K. (2001). The mechanism of glycerol conduction in aquaglyceroporins. Structure *9*, 1083–1093.

Jo, S., Kim, T., Iyer, V.G., and Im, W. (2008). CHARMM-GUI: a web-based graphical user interface for CHARMM. J. Comput. Chem. *29*, 1859–1865.

Kabsch, W. (2010). Xds. Acta Crystallogr. D Biol. Crystallogr. *66*, 125–132.

Katano, T., Ito, Y., Ohta, K., Yasujima, T., Inoue, K., and Yuasa, H. (2014a). Competitive inhibition of AQP7-mediated glycerol transport by glycerol derivatives. Drug Metab. Pharmacokinet. *29*, 348–351.

Katano, T., Ito, Y., Ohta, K., Yasujima, T., Inoue, K., and Yuasa, H. (2014b). Functional characteristics of aquaporin 7 as a facilitative glycerol carrier. Drug Metab. Pharmacokinet. *29*, 244–248.

Klauda, J.B., Venable, R.M., Freites, J.A., O'connor, J.W., Tobias, D.J., Mondragon-Ramirez, C., Vorobyov, I., MacKerell, A.D., Jr., and Pastor, R.W. (2010). Update of the CHARMM all-atom additive force field for lipids: validation on six lipid types. J. Phys. Chem. B *114*, 7830–7843.

Kondo, H., Shimomura, I., Kishida, K., Kuriyama, H., Makino, Y., Nishizawa, H., Matsuda, M., Maeda, N., Nagaretani, H., Kihara, S., et al. (2002). Human aquaporin adipose (AQPap) gene. Genomic structure, promoter analysis and functional mutation. Eur. J. Biochem. *269*, 1814–1826.

Laforenza, U., Scaffino, M.F., and Gastaldi, G. (2013). Aquaporin-10 represents an alternative pathway for glycerol efflux from human adipocytes. PLoS One *8*, e54474.

Le Lay, S., Briand, N., and Dugail, I. (2015). Adipocyte size fluctuation, mechano-active lipid droplets and caveolae. Adipocyte *4*, 158–160.

Lee, J.K., Kozono, D., Remis, J., Kitagawa, Y., Agre, P., and Stroud, R.M. (2005). Structural basis for conductance by the archaeal aquaporin AqpM at 1.68 A. Proc. Natl. Acad. Sci. U S A *102*, 18932–18937.

Londos, C., Brasaemle, D.L., Schultz, C.J., Segrest, J.P., and Kimmel, A.R. (1999). Perilipins, ADRP, and other proteins that associate with intracellular neutral lipid droplets in animal cells. Semin. Cell Dev. Biol. *10*, 51–58.

MacKerell, A.D., Jr., Bashford, D., Bellott, M., Dunbrack, R.L., Jr., Evanseck, J.D., Field, M.J., Fischer, S., Gao, J., Guo, H., and Ha, S. (1998). All-atom empirical potential for molecular modeling and dynamics studies of proteins. J. Phys. Chem. B *102*, 3586–3616.

Maeda, N., Funahashi, T., Hibuse, T., Nagasawa, A., Kishida, K., Kuriyama, H., Nakamura, T., Kihara, S., Shimomura, I., and Matsuzawa, Y. (2004). Adaptation to fasting by glycerol transport through aquaporin 7 in adipose tissue. Proc. Natl. Acad. Sci. U S A *101*, 17801–17806.

McCoy, A.J., Grosse-Kunstleve, R.W., Adams, P.D., Winn, M.D., Storoni, L.C., and Read, R.J. (2007). Phaser crystallographic software. J. Appl. Crystallogr. *40*, 658–674.

Miranda, M., Escote, X., Ceperuelo-Mallafre, V., Alcaide, M.J., Simon, I., Vilarrasa, N., Wabitsch, M., and Vendrell, J. (2010). Paired subcutaneous and visceral adipose tissue aquaporin-7 expression in human obesity and type 2 diabetes: differences and similarities between depots. J. Clin. Endocrinol. Metab. *95*, 3470–3479.

Newby, Z.E., O'connell, J., 3rd, Robles-Colmenares, Y., Khademi, S., Miercke, L.J., and Stroud, R.M. (2008). Crystal structure of the aquaglyceroporin PfAQP from the malarial parasite *Plasmodium falciparum*. Nat. Struct. Mol. Biol. *15*, 619–625.

Nieman, K.M., Kenny, H.A., Penicka, C.V., Ladanyi, A., Buell-Gutbrod, R., Zillhardt, M.R., Romero, I.L., Carey, M.S., Mills, G.B., Hotamisligil, G.S., et al. (2011). Adipocytes promote ovarian cancer metastasis and provide energy for rapid tumor growth. Nat. Med. *17*, 1498–1503.

Palmgren, M., Hernebring, M., Eriksson, S., Elbing, K., Geijer, C., Lasic, S., Dahl, P., Hansen, J.S., Topgaard, D., and Lindkvist-Petersson, K. (2017). Quantification of the intracellular life time of water molecules to measure transport rates of human aquaglyceroporins. J. Membr. Biol. *250*, 629–639.

Parrinello, M., and Rahman, A. (1981). Polymorphic transitions in single crystals: a new molecular dynamics method. J. Appl. Phys. *52*, 7182–7190.

Rodriguez, A., Catalan, V., Gomez-Ambrosi, J., Garcia-Navarro, S., Rotellar, F., Valenti, V., Silva, C., Gil, M.J., Salvador, J., Burrell, M.A., et al. (2011). Insulin- and leptin-mediated control of aquaglyceroporins in human adipocytes and hepatocytes is mediated via the PI3K/Akt/mTOR signaling cascade. J. Clin. Endocrinol. Metab. *96*, E586–E597.

Smart, O.S., Neduvelil, J.G., Wang, X., Wallace, B.A., and Sansom, M.S. (1996). HOLE: a program for the analysis of the pore dimensions of ion channel structural models. J. Mol. Graph. *14*, 354–360, 376.

Terwilliger, T.C., Grosse-Kunstleve, R.W., Afonine, P.V., Moriarty, N.W., Zwart, P.H., Hung, L.W., Read, R.J., and Adams, P.D. (2008). Iterative model building, structure refinement and density modification with the PHENIX AutoBuild wizard. Acta Crystallogr. D Biol. Crystallogr. *64*, 61–69.

Wallace, A.C., Laskowski, R.A., and Thornton, J.M. (1995). LIGPLOT: a program to generate schematic diagrams of protein-ligand interactions. Protein Eng. *8*, 127–134.

Winn, M.D., Ballard, C.C., Cowtan, K.D., Dodson, E.J., Emsley, P., Evans, P.R., Keegan, R.M., Krissinel, E.B., Leslie, A.G., Mccoy, A., et al. (2011). Overview of the CCP4 suite and current developments. Acta Crystallogr. D Biol. Crystallogr. *67*, 235–242.

Wu, E.L., Cheng, X., Jo, S., Rui, H., Song, K.C., Dávila-Contreras, E.M., Qi, Y., Lee, J., Monje-Galvan, V., and Venable, R.M. (2014). CHARMM-GUI membrane builder toward realistic biological membrane simulations. J. Comput. Chem. *35*, 1997–2004.

STAR★METHODS

KEY RESOURCES TABLE

REAGENT or RESOURCE	SOURCE	IDENTIFIER
Chemicals, Peptides, and Recombinant Proteins		
6xHis-hAQP7(aa33-279)	Hansen et al., 2016	n/a
n-Dodecyl-β-D-Maltopyranoside (DDM)	Anatrace	Cat#D310S; CAS: 69227-93-6
Ni-NTA agarose	Invitrogen	Cat#:R90115
Octyl Glucose Neopentyl Glycol (OGNG)	Anatrace	Cat#NG311, CAS: 1257853-32-9
n-octyl-β-D-glucopyranoside	Detergent screen, Hampton Research	Cat#HR2-408; detergent#56; CAS: 29836-26-8
Deposited Data		
Crystal structure of AQP7 at 1.9 Å	This study	PDB: 6QZI https://rcsb.org
Crystal structure of AQP7 at 2.2 Å	This study	PDB: 6QZJ https://rcsb.org
Structure of human AQP10	Gotfryd et al., 2018	PDB:: 6f7h
Structure of *E. coli* glycerol uptake facilitator protein GlpF	Fu et al., 2000	PDB: 1fx8
Structure of *Plasmodium falciparum* aquaporin PfAQP	Newby et al., 2008	PDB: 3c02
Structure of archeal aquaporin AqpM	Lee et al., 2005	PDB: 2f2b
Software and Algorithms		
XDS	Kabsch, 2010	http://xds.mpimf-heidelberg.mpg.de
CCP4	Winn et al., 2011	https://www.ccp4.ac.uk
Phenix version 1.14	Adams et al., 2010	http://www.phenix-online.org
Coot	Emsley et al., 2010	https://www2.mrc-lmb.cam.ac.uk/personal/pemsley/coot/
HOLE	Smart et al., 1996	http://www.holeprogram.org
PyMOL	The PyMOL Molecular Graphics System, Version 2.0 Schrödinger, LLC	https://pymol.org/2/
LigPlot+	Wallace et al., 1995	https://www.ebi.ac.uk/thornton-srv/software/LigPlus/
Gromacs	Abraham et al., 2015	http://www.gromacs.org
Other		
P. pastoris GS115 *aqy1Δ::HIS4 agp1Δ::NatMX* expressing 6xHis-hAQP7(aa33-279)	Hansen et al., 2016	n/a

LEAD CONTACT AND MATERIALS AVAILABILITY

Further information and requests for resources and reagents should be directed to and will be fulfilled by the Lead Contact, Karin Lindkvist-Petersson (karin.lindkvist@med.lu.se).

This study did not generate new unique reagents.

EXPERIMENTAL MODEL AND SUBJECT DETAILS

Heterologous Protein Expression

Human AQP7 (aa33-279) with C-terminal 6 His-tag was expressed in a *Komagataella pastoris* (previously known as *Pichia pastoris*) strain (GS115 *aqy1Δ::HIS4 agp1Δ::NatMX*) without endogenous aquaporins and aquaglyceroporins, the construct was generated in a previous study (Hansen et al., 2016). Cells from a glycerol stock were taken up and plated on YPD agar for 3 days, followed by growth in shaker flasks o/n, 180 rpm. A 25 ml pre-culture was inoculated with colonies from the YPD agar plate in buffered glycerol complex medium (BMGY) (1 % w/v yeast extract, 2 % w/v peptone, 100 mM potassium phosphate pH 6.0, 1.34 % w/v yeast nitrogen base, 0.4 mg/l biotin, 1 % v/v glycerol). A 200 ml BMGY culture was inoculated with cells from the 25 ml culture and grown o/n to

an optical density of A_{600} = 5. Protein expression was induced by centrifugation and resuspension of cells in 1 l buffered methanol complex medium (1 % *w/v* yeast extract, 2 % *w/v* peptone, 100 mM potassium phosphate pH 6.0, 1.34 % *w/v* yeast nitrogen base, 0.4 mg/l biotin, 0.5 % *v/v* methanol). The induction time was 27-30 h, supplementing the culture with 0.5 % v/v methanol after 24 h. All steps were performed at 30°C.

METHOD DETAILS

Protein Purification

Cells were disrupted by high-pressure homogenization (Biox AB, Sweden) and the lysate was supplemented with EDTA-free protease inhibitor cocktail (Roche) and cleared (4000 *g*, 10 min, 4°C) before isolating membranes by centrifugation (145 000 *g*, 90 min, 4°C). Crude membranes were homogenized in 20 mM NaOH followed by centrifugation (145 000 *g*, 90 min, 4°C) and the washed membrane pellet was homogenized in a solubilization buffer (20 mM sodium phosphate pH 8.0, 300 mM NaCl, 10 % v/v glycerol, 1 mM DTT). AQP7 was extracted by 1 % w/v n-Dodecyl-β-D-Maltopyranoside (DDM) (Anatrace) for 2 h at 4°C under gentle stirring. Non-solubilized fraction was removed by centrifugation (145 000 *g*, 30 min, 4°C), supernatant diluted 5-fold with solubilization buffer and incubated with nickel affinity resin (Ni-NTA agarose, Qiagen) overnight in presence of 5 mM imidazole. All purification steps were performed at 4°C. The resin was washed with 10 BV buffer A (20 mM sodium phosphate, 300 mM NaCl, 20 % v/v glycerol, 0.07 % w/v Octyl Glucose Neopentyl Glycol (OGNG) (Anatrace)) containing 10 mM imidazole and 10 BV buffer A containing 30 mM imidazole. The protein was eluted by 3 BV buffer A containing 300 mM imidazole, concentrated with 100 kDa molecular weight cutoff Amicon Ultra centrifugal filters (Merck) and loaded onto a Superdex 200 Increase 10/300 GL column (GE Healthcare) equilibrated with buffer B (20 mM sodium phosphate pH 7.5, 100 mM NaCl, 5 % v/v glycerol, 0.07 % w/v OGNG). Purity of elution fractions was evaluated by SDS-PAGE (NuPage 4-12 % Bis-Tris gel, Invitrogen) stained with SimplyBlue SafeStain (Invitrogen).

Crystallization and Structure Determination

Crystallization

The purified AQP7 was crystallized at 4°C by hanging drop vapor diffusion using a protein to precipitant solution ratio of 1:2. The protein concentration was 9 mg/ml and the precipitant solution contained 85 mM Tris pH 8.0, 37 % v/v PEG 200 and 0.80 % v/v n-octyl-β-D-glucopyranoside (Hampton Research).

Data Collection

Crystal 1 (1.9 Å) was subjected to a gradient increase of glycerol to 20 % in 5 % increments in the mother liquor before plunge freezing in liquid nitrogen as a way of crude dehydration. Crystal 2 (2.2 Å) was only subjected to 5 % glycerol in the mother liquor before plunge freezing. Both crystals used for data collection were grown in the same crystallization drop. Diffraction data was collected at the P13 beamline at PETRA III, the European Molecular Biology Laboratory, Deutsches Elektronen-Synchrotron, amburg, Germany (Cianci et al., 2017) under cryo-conditions using a PILATUS 6M detector. Two data sets were collected from single crystals.

Structure Determination, Refinement and Validation

The data sets were processed using XDS (Kabsch, 2010) and aimless (Evans, 2006, 2011) within the CCP4 progam suite (Winn et al., 2011). Molecular replacement (MR) was performed using Phaser (McCoy et al., 2007) in PHENIX (Adams et al., 2010) with one monomer of human AQP10 (PDB: 6f7h) as a search model, and initial model building was performed using PHENIX AutoBuild (Terwilliger et al., 2008). Manual model building and iterative refinement with TLS parameters and isotropic B-factors were performed using Coot (Emsley et al., 2010) and phenix.refine (Afonine et al., 2012), respectively. To evaluate the extended electron density present in the pore in proximity to the NPA region, glycerol or PEG 200 were modeled into it. The dimensions of the electron density, omit maps and potential hydrogen bonds to surrounding residues (Table S1), support that modeling glycerol molecules is one correct interpretation of the electron density. Two alternative glycerol molecules and respective alternative water molecules were linked as a constrained group for the occupancy refinement. One loop region of the 1.9 Å model (Gln145 – Ala153) had poorly defined electron density and was built guided by the 2.2 Å model. Model validation was performed using the MolProbity (Chen et al., 2010) in PHENIX. Ramachandran statistics are similar in both structures, with 0.82 % outliers, which comprise 2 out of a total of 247 residues. The outliers correspond to Y223 and I225 in the selectivity filter area. The density for both residues is well-defined and trustworthy at the resolution obtained. All the structure figures including visualization of the HOLE analysis were generated in PyMOL (Schrödinger). The 2D representation which was prepared in LigPlot+ (Wallace et al., 1995).

HOLE Analysis of the Pore

The pore radius calculations and analysis were performed using the program HOLE (Smart et al., 1996), obtained from www.holeprogram.org. The coordinates of AQP10 (PDB: 6f7h, molA) and GlpF (PDB:1fx8) were superimposed on the AQP7 structure (1.9 Å), and non-protein atoms were removed from the files. HOLE was run with cpoint coordinates (a point within the channel) defined as the C1 atom of the G4a glycerol in the AQP7 structure. Although the pores follow the direction of the z axis (0, 0, 1), the most narrow pore radius of 0.9 Å for AQP10 previously reported (Gotfryd et al., 2018) could only be achieved when providing a cvect (direction along the channel) of (1, 1, 3), which was used for analysis of all structures. The pore positions versus pore radii were plotted in Microsoft Excel.

Molecular Dynamics Simulations

MD simulations were carried out in the Gromacs simulation suite, version 2018 (Abraham et al., 2015) using the Charmm36m force field (Huang et al., 2017). The initial setup was prepared using Charmm-GUI (Jo et al., 2008; Wu et al., 2014) embedding the AQP7 tetramer in a lipid bilayer patch of 121 POPC lipids (Klauda et al., 2010) and surrounded by 10910 CHARMM TIP3P water molecules (MacKerell et al., 1998). 24 potassium and 32 chloride atoms were added to ensure charge neutrality and to reach an ionic strength of 150 mM. 3 simulation systems were prepared: without glycerol, with 16 glycerol (4 per monomer) bound to the crystallographic positions, and with 16 glycerol molecules initially placed in bulk solvent. For each setup, 5 replicas were run with a length ranging from 500 to 1000 ns. Assuming independent monomers, this corresponds to N=20 statistics for the analysis of water permeation events. Hydrogen-involving bonds were constrained using LINCS (Hess et al., 1997), allowing for an integration time step of 2 fs. The van der Waals interactions were force-switched from 0.8 to 1.2 nm. Electrostatic interactions were treated using particle mesh Ewald (Darden et al., 1993) using a real-space cut-off of 1.2 nm. The velocity-rescale thermostat (Bussi et al., 2007) and Parrinello-Rahman barostat (Parrinello and Rahman, 1981) were used to control the temperature and pressure at 300K and 1 bar, with a coupling constant of 1.0 and 5.0 ps, respectively. The PMF profile was estimated from the number density of the central glycerol carbon along the Z-direction and applying the Boltzmann relation. The first 100 ns of each replica were discarded from this analysis for equilibration.

QUANTIFICATION AND STATISTICAL ANALYSIS

Software

Structure Determination and Validation

XDS (Kabsch, 2010), aimless (Evans, 2006, 2011) within the CCP4 progam suite (Winn et al., 2011), Phaser (McCoy et al., 2007) in PHENIX (Adams et al., 2010), PHENIX AutoBuild (Terwilliger et al., 2008), Coot (Emsley et al., 2010), phenix.refine (Afonine et al., 2012), MolProbity (Chen et al., 2010).

Structure Analysis and Visualization

HOLE (Smart et al., 1996), Microsoft Excel, PyMOL (Schrödinger), LigPlot+ (Wallace et al., 1995).

Molecular Dynamics Simulations

Gromacs simulation suite, version 2018 (Abraham et al., 2015), Charmm-GUI (Jo et al., 2008; Wu et al., 2014).

Diffraction Data Collection and Final Refinement

Diffraction data collection and final refinement statistics are summarized in Table 1.

Statistical Analysis Molecular Dynamics Simulations

For each MD setup, 5 replicas were run and assuming independent monomers, this corresponds to N=20 statistics for the analysis of water permeation events (Figure 3A).

DATA AND CODE AVAILABILITY

Coordinates for the structure of AQP7 are deposited in the Protein Data Bank (http://www.rcsb.org) with accession numbers PDB: 6qzi (1.9 Å resolution) and PDB: 6qzj (2.2 Å resolution).

ADDITIONAL RESOURCES

This study has not generated or contributed to a new website/forum.